

Speckle noise reduction for structural vibration measurement with laser Doppler vibrometer on moving platform

Zeng, Yuanchen; Nunez, Alfredo; Li, Zili

DOI

[10.1016/j.ymssp.2022.109196](https://doi.org/10.1016/j.ymssp.2022.109196)

Publication date

2022

Document Version

Final published version

Published in

Mechanical Systems and Signal Processing

Citation (APA)

Zeng, Y., Nunez, A., & Li, Z. (2022). Speckle noise reduction for structural vibration measurement with laser Doppler vibrometer on moving platform. *Mechanical Systems and Signal Processing*, 178, Article 109196. <https://doi.org/10.1016/j.ymssp.2022.109196>

Important note

To cite this publication, please use the final published version (if applicable). Please check the document version above.

Copyright

Other than for strictly personal use, it is not permitted to download, forward or distribute the text or part of it, without the consent of the author(s) and/or copyright holder(s), unless the work is under an open content license such as Creative Commons.

Takedown policy

Please contact us and provide details if you believe this document breaches copyrights. We will remove access to the work immediately and investigate your claim.



Speckle noise reduction for structural vibration measurement with laser Doppler vibrometer on moving platform

Yuanchen Zeng, Alfredo Núñez, Zili Li ^{*}

Section of Railway Engineering, Faculty of Civil Engineering and Geosciences, Delft University of Technology, Stevinweg 1, Delft, the Netherlands

ARTICLE INFO

Communicated by: Spiliotis Fassois

Keywords:

Laser Doppler vibrometer
Laser Doppler vibrometer on moving platform
Speckle noise
Spike detection
Imputation
Railway track

ABSTRACT

Speckle noise is a major problem for structural vibration measurements with Laser Doppler vibrometer on moving platform (LDVom) due to its highly random, frequent, and broadband nature, especially at high speeds. This paper develops a new post-processing framework to reduce speckle noise based on a case study of LDVom measurements on railway tracks. First, the characteristics of the speckle noise are studied. As the speed increases, the speckle noise occurs more frequently, with shorter intervals, shorter durations, greater amplitudes, and broader frequency bands. Then, a three-step despeckle framework is proposed, consisting of spike detection, imputation, and smoothing. This framework works by detecting and replacing spikes, recovering false positives, and smoothing false negatives and residual noise. To showcase this framework, we use a wavelet-based method for Step 1, an ARIMA-based method for Step 2, and a Butterworth filter for Step 3. Besides, the parameter selection strategies and the alternative methods are discussed. Next, the methods are validated through qualitative comparison and quantitative evaluation using a Monte Carlo-based strategy. We demonstrate that the proposed methods effectively reduce the speckle noise at speeds of at least 20 km/h while avoiding the pseudo vibrations. Finally, we show that the LDVom successfully captures the track vibrations at dominant frequencies of 500 ~ 700 Hz with good repeatability between different laps and good agreement with trackside measurements.

1. Introduction

Laser Doppler vibrometer (LDV) is a laser-based sensing instrument that measures the vibration velocity of a target based on Doppler frequency shift. The non-contact sensing nature of LDV has the advantages of accessing places unsuitable for contact-based sensors, measuring different objects or locations with the same instrumentation, and avoiding the influence of sensors on target dynamics. LDV has been successfully applied to modal tests, system identification, and damage detection of many engineering structures, as summarised in [1–3].

Speckle noise has been reported as a major problem in the applications of LDV [1–3]. In signals measured by an LDV, speckle noise appears as random spikes in time and broadband noise floor in spectra [3]. The source of speckle noise is speckle patterns that appear

Abbreviations: LDV, laser Doppler vibrometer; LDVom, laser Doppler vibrometer on moving platform; CWT, continuous wavelet transform; DWT, discrete wavelet decomposition; IDWT, inverse discrete wavelet transform; ARIMA, autoregressive integrated moving average; ACF, autocorrelation function; SVM, support vector machine; ANN, artificial neural network.

^{*} Corresponding author.

E-mail addresses: Y.Zeng-2@tudelft.nl (Y. Zeng), A.A.NunezVicencio@tudelft.nl (A. Núñez), Z.Li@tudelft.nl (Z. Li).

<https://doi.org/10.1016/j.ymssp.2022.109196>

Received 19 October 2021; Received in revised form 2 February 2022; Accepted 19 April 2022

Available online 29 May 2022

0888-3270/© 2022 The Author(s). Published by Elsevier Ltd. This is an open access article under the CC BY-NC-ND license (<http://creativecommons.org/licenses/by-nc-nd/4.0/>).

when a laser beam is projected on an optically rough surface [1,3]. The severity of speckle noise depends not only on laser and target properties but also on the change of speckle patterns due to the relative motion between laser and target [1,3]. Therefore, different measurement setups of LDV have different severity of speckle noise. Depending on the number of measurement locations, we classify LDV measurement setups into discrete measurement (at one or multiple discrete locations) and continuous measurement (along a continuous path). In the past years, both manufacturers and users have made great efforts to try to address the problem of speckle noise. Table 1 summarises the influence and the mitigation approaches of speckle noise for different setups from the literature.

Compared to the setups in the discrete measurement category, speckle noise is more troublesome for the setups in the continuous measurement category due to the drastic change of speckle patterns caused by the relative motion between laser spot and target. Speckle noise becomes more severe at higher speeds or on rougher surfaces.

Table 1 divides the approaches mitigating speckle noise into three levels – the equipment, measurement, and post-processing. At the equipment level, innovations in LDV technology have shown their potential to reduce speckle noise in different measurement setups [13–20]. These advances enable users to improve the quality of measured signals by properly selecting LDV equipment. At the measurement level, users can mitigate speckle noise by optimising the settings. Since LDVom is intended for measuring large-scale structures, lowering the moving speed can reduce speckle noise but at the cost of efficiency. In cases where the structural response depends on the dynamic loading of the moving platform, lower speeds result in smaller vibrations. Additionally, for LDVom measurements on working surfaces or large-scale structures, treating the surface to reduce speckle noise is not possible or is expensive.

Further, speckle noise can be reduced at the post-processing level. It is noteworthy that some approaches at the equipment level also contain signal processing methods, e.g., the signal combining method [13,16–19] and the tracking filter [20,21]. These methods are usually integrated with the equipment and implemented in real-time. The post-processing level in Table 1 represents the efforts made after signal acquisition. The three levels of approaches should be combined to achieve the best signal quality, especially in challenging situations.

For continuous scanning LDV, the availability of repeated measurements allows speckle noise reduction, such as by averaging multiple measurements or neglecting the frequencies related to the scanning frequency [22]. However, for LDVom measurements on large-scale structures or structures under random or time-varying excitations, repeated measurements are not possible or are expensive, so post-processing is necessary to reduce speckle noise. Many conventional filtering or denoising methods are available. However, since they are not specifically designed to handle speckle noise, they may provide unsatisfactory performance [36]. For example, low-pass filters can reduce speckle noise amplitude but degrade its sharpness [24].

So far, many methods have been developed to eliminate two-dimensional speckle noise in digital holography or synthetic aperture radar images [37,38], but only a few methods have been proposed to reduce speckle noise in time series. In [5], a kurtosis ratio is used to detect speckle noise and select the undistorted part of a signal. In [9], speckle noise is detected by using short-time energy and kurtosis and further removed through linear prediction. However, the methods in [5] and [9] are developed for single-point LDV setups, which might not be applicable to continuous measurements where speckle noise occurs more frequently. In [30], speckle noise is detected based on high-pass filtering or wavelet transform and removed through interpolation or curve fitting. In [35], speckle noise is detected based on the kurtosis ratio and removed through linear prediction. In [36], speckle noise is reduced by using empirical wavelet transform. The methods in [30], [35] and [36] are tested at the scanning speed of 5 cm/s, 1 cm/s, and 10 cm/s, respectively, where the speckle noise is less severe than that in high-speed measurements. Nevertheless, the above methods can potentially be adapted and used in our proposed solution for speckle noise reduction (see Appendix).

This background motivates us to develop a new post-processing framework for speckle noise reduction, especially for high-speed LDVom measurements with severe speckle noise. The LDVom measurement on a railway track structure is used as a case study, in which the laser spot scans along the track and measures its vibration induced by the moving platform at speeds up to 20 km/h. This setup can be applied to track condition monitoring since track component properties affect track vibrations [39,40]. Meanwhile, the proposed methods are adaptable to different kinds of structural vibration measurements, e.g., on pavements, bridges, and tunnels.

The remainder of this paper is organised as follows. In Section 2, speckle noise samples are collected from LDVom measurements, and their characteristics are investigated. In Section 3, a three-step despeckle framework is proposed. To showcase this framework, we develop a wavelet-based spike detection method for Step 1, an ARIMA-based imputation method for Step 2, and a traditional smoothing filter for Step 3. Moreover, the alternative methods at different steps are discussed in Appendix. In Section 4 and Section 5, stepwise validation and verification are performed, respectively. Finally, the conclusions are summarised.

2. Characteristics of the speckle noise

2.1. LDVom measurements in the laboratory

The experimental setup in Fig. 1 is designed for LDVom measurements on the V-Track test rig that resembles a vehicle-track structure [41,42]. The track structure consists of rails, sleepers, track slabs, and fastening systems. Above the track, a beam is driven by a motor to rotate around the central axis of the test rig. On the end of the beam, a suspension system loads a wheel in the vertical direction, placing it into contact with the rail.

A one-dimensional LDV (Polytec RSV-150) is mounted on the beam near its rotation axis. A mirror is fixed on the end of the beam to direct the laser onto the track. As the beam rotates, the wheel rolls along the rail and the laser spot scans along the track structure, which enables vibration excitation and scanning measurement simultaneously. Besides, there are four rail joints in the test rig. When the wheel rolls over the joints, impacts occur. In our measurement setting, the sampling frequency is 102,400 Hz, the static wheel load is 4,000 N, and the sensitivity of the LDV is 100 mm/s/V.

Table 1

Speckle noise in different LDV measurement setups from the literature.

Categories	Measurement setups	Influence of speckle noise	Mitigation approaches of speckle noise		
			Equipment level	Measurement level	Post-processing level
Discrete measurement	<p>Single-point LDV: The laser spot is targeted at a fixed point on a vibrating object [4–9].</p>	<ul style="list-style-type: none"> Some of the literature encounters the speckle noise problem, e.g., in [4,5,8–10,12]. Speckle noise occurs locally and occasionally. 	<ul style="list-style-type: none"> A tracking LDV with controlled mirrors to reduce the relative motion between laser and target [8]. 	<ul style="list-style-type: none"> Treat the target surface with retroreflective tape [4]. 	<ul style="list-style-type: none"> Use filters or post-processing methods, e.g., kurtosis ratio-based method [5], Gaussian filter [6], decorrelation and linear prediction-based method [9], median filter [10], and averaging [11].
	<p>Stepped scanning LDV: The laser spot scans an object along selected points stepwise and dwells at each point for a specific duration [10–12]. Most setups are used for modal analysis.</p>		<p>(Applicable to all setups mentioned)</p> <ul style="list-style-type: none"> Advanced LDV designs, e.g., adaptive optics [13,14] and scanning average based on a high-frequency scanner [15]. 		
Continuous measurement	<p>Continuous scanning LDV: The laser spot repeatedly scans an object along a closed path. Most setups are applied to modal analysis [22–30].</p>	<ul style="list-style-type: none"> Most of the literature encounters the speckle noise problem. Speckle noise is nearly periodic at the scanning frequency and its harmonics due to repeated closed-path scanning [22,24,25,29]. Speckle noise gets more severe at higher scanning frequencies or on rougher surfaces. 	<ul style="list-style-type: none"> Signal diversity techniques, e.g., combining signals from multiple detector channels, [13,16,17] or multiple laser heads [18,19]. Built-in filters, e.g., tracking filter [20,21]. 	<ul style="list-style-type: none"> Adjust the measurement settings, e.g., the scanning frequency [22,25,26,29], the measurement length [28,29], and the distance between LDV and target [29]. Treat the target surface with retroreflective tape [27]. 	<ul style="list-style-type: none"> Smooth the identified mode shapes [26–28]. Use post-processing methods, e.g., windowing [25] and wavelet or high-pass filtering-based spike removal [30].
	<p>LDV on moving platform (LDVom): An LDV is mounted on a moving platform, and its laser spot scans an object continuously along an open path [21,31–35]. Most setups are intended for large-scale structures, on which repeated measurements are usually not possible or are expensive.</p>		<ul style="list-style-type: none"> Most of the literature encounters the speckle noise problem. Speckle noise is highly irregular. Speckle noise gets more severe at higher moving speeds or on rougher surfaces. 	<ul style="list-style-type: none"> A mobile LDV with a large spot size [33]. 	

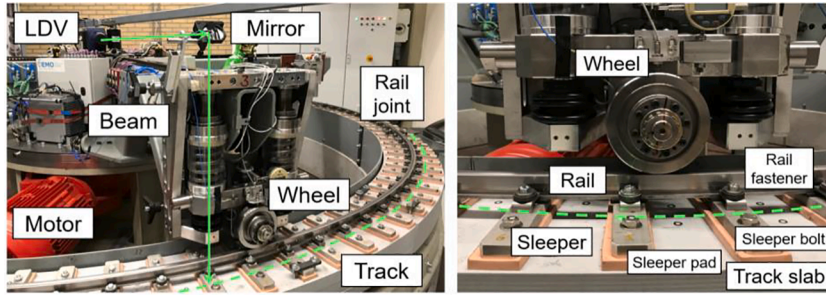


Fig. 1. LDVom measurement setup on the test rig. The green arrows represent the laser beam, and the green dashes represent the path of the laser spot.

2.2. Characteristics in the time domain

Gaining insights into the speckle noise is the first step towards reducing it. In the time domain, speckle noise appears as random spikes. First, we manually label more than one thousand spike samples from LDVom measurements at three speeds – 0.5 km/h, 5 km/h, and 20 km/h. This method is reliable when spikes behave differently from genuine vibrations. Fig. 2 shows a sample of LDVom measurement with seven spikes labelled. We define three features to characterise a spike in the time domain – interval, duration, and amplitude. A spike interval is the time difference between two adjacent spikes, denoted as b . A spike duration is the time difference between the boundaries of a spike (e.g., Points A and B), denoted as l . A spike amplitude, denoted as h , is the difference between the local peak or valley of a spike (e.g., Point C) and the average amplitude of its boundaries (e.g., Points A and B). Spike amplitude is positive for a peak whereas negative for a valley.

The distribution of each feature is estimated based on the relative frequency of its values in consecutive and non-overlapping bins within the total number of samples. As shown in Fig. 3(a)–(c), the distributions of spike intervals, durations, and amplitudes at different speeds reflect the randomness of the speckle noise. At higher moving speeds, spikes occur more frequently with shorter durations and larger amplitudes. The amplitude distributions of the peaks are similar to those of the valleys. In addition, the duration of each spike is plotted against its amplitude in Fig. 3(d). The hyperbolic shape shows that a spike is more likely to be shorter in duration if it is greater in amplitude and vice versa.

2.3. Characteristics in the frequency domain

Considering the discreteness and nonstationarity of the speckle noise, we adopt continuous wavelet transform (CWT) with Morlet wavelet [43] to study its characteristics in the frequency domain. Fig. 4 shows the spectrograms for the three samples of LDVom signals at different speeds. It shows that spikes are discrete in time and broadband in frequency. As the speed increases, the frequency band is broader since the spike duration is shorter and the spike amplitude is larger. Additionally, the low-frequency parts of a spike may overlap with genuine vibrations or adjacent spikes.

The above characteristics of speckle noise in time and frequency domains not only account for the limited performance of conventional filters but also motivate the development of new despeckle methods. The parameter selection in the proposed despeckle methods requires some prior estimates of spike characteristics. Instead of manual spike collection, a fast approach is to directly observe an LDV signal and roughly estimate the features of spikes, e.g., the average spike duration \bar{l} and the minimum spike amplitude h_{\min} .

3. Despeckle methodology

When applying conventional methods to despeckle, such as a low-pass filter, both spikes and genuine vibrations are affected, and the amplitude of spikes can be shortened but not eliminated. It is more problematic when speckle noise overlaps with genuine vibrations in the frequency band of interest, leading to severe residual noise and causing confusion in signal interpretation [24]. Therefore, we propose a new despeckle framework, which consists of three steps:

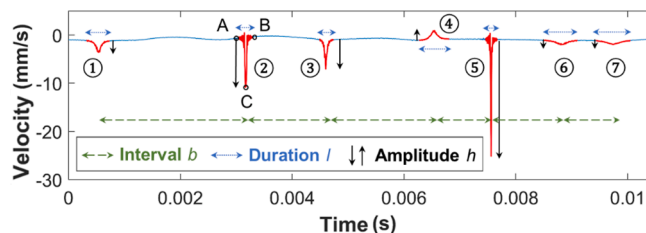


Fig. 2. A sample of LDVom measurement with labelled spikes (0.5 km/h).

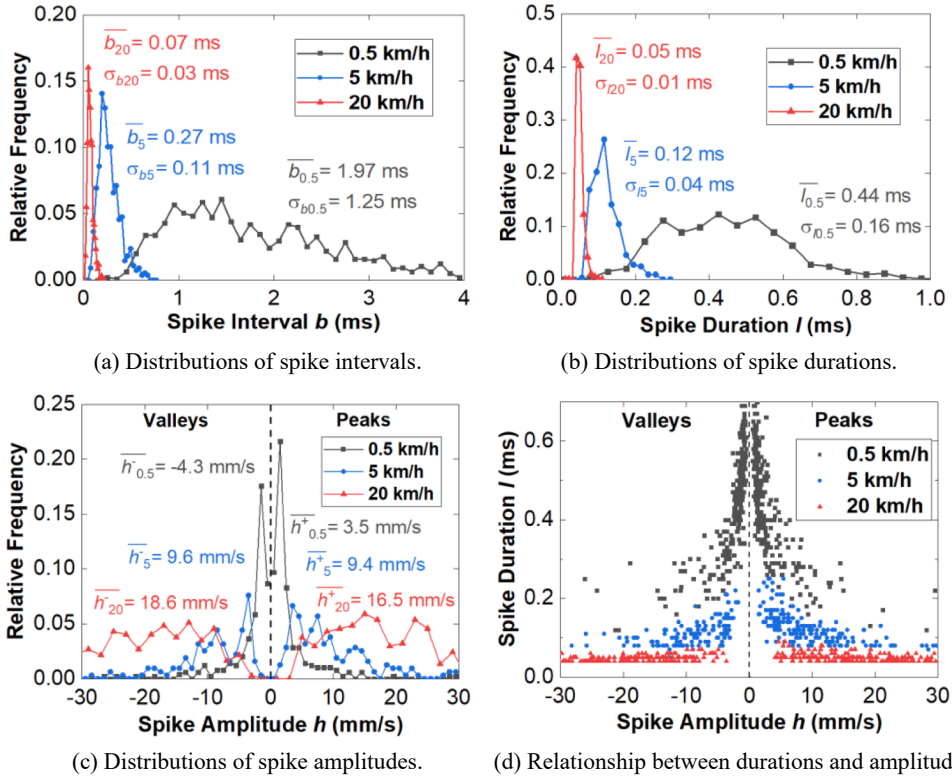


Fig. 3. Time-domain characteristics of the speckle noise. $\bar{b}_v, \bar{l}_v, \bar{h}_v^+, \bar{h}_v^-$ denote the means of spike intervals, spike durations, peak amplitudes, and valley amplitudes at speed v , respectively; σ_{b_v} and σ_{l_v} denote the standard deviations of spike intervals and spike durations at speed v , respectively.

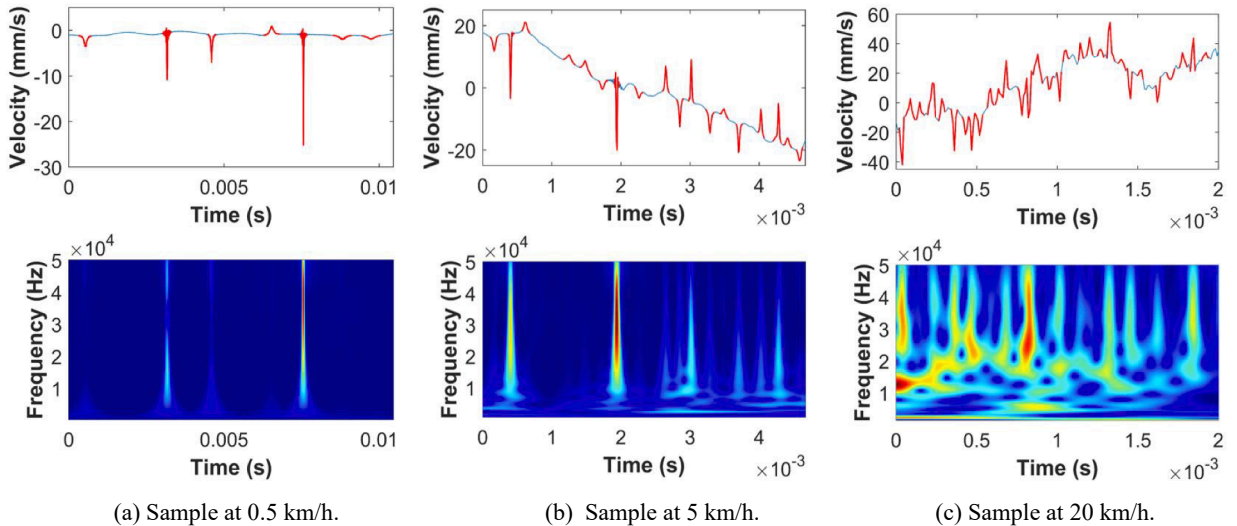


Fig. 4. Frequency-domain characteristics of the speckle noise.

- Step 1. Spike detection: distinguish spikes from genuine vibrations.
- Step 2. Imputation: replace spikes based on time series modelling and predictions.
- Step 3. Smoothing: filter out residual noise.

The main feature of this framework is that spikes are detected and replaced before being filtered. To showcase how these steps work, we propose a specific method for each of the three steps. Although these methods are used in the case study on railway tracks,

they are adaptable to other structural vibration measurements. Moreover, the alternative methods at different steps and their pros and cons are discussed in [Appendix](#).

3.1. Step 1: Spike detection

Step 1 aims to detect spikes in LDV signals based on their characteristics. In this section, we propose a wavelet-based spike detection method.

3.1.1. Wavelet decomposition and reconstruction

As a tool for processing nonstationary signals, wavelet transform breaks up a signal into shifted and scaled wavelets. The discrete wavelet decomposition (DWT) of a time series u consists of convolving u with two orthogonal filters (a low-pass filter LoF and a high-pass filter HiF) and downsampling the results by two [44], as expressed by the following operator pair:

$$\begin{cases} DWT_A(u) = (u * LoF) \downarrow 2 \\ DWT_D(u) = (u * HiF) \downarrow 2 \end{cases} \quad (1)$$

where DWT_A and DWT_D correspond to the outputs of the low-pass filter and the high-pass filter, respectively, $*$ denotes the convolution operator, and \downarrow denotes the downsampling operator. Based on (1), the DWT of a signal x produces two series of wavelet coefficients:

$$\begin{cases} cA_1 = DWT_A(x) \\ cD_1 = DWT_D(x) \end{cases} \quad (2)$$

where cA_1 are the approximation coefficients and cD_1 are the detail coefficients [44]. The approximation coefficients can be further decomposed through DWT as follows.

$$\begin{cases} cA_{k+1} = DWT_A(cA_k) \\ cD_{k+1} = DWT_D(cA_k) \end{cases} \quad k = 1, 2, \dots \quad (3)$$

where cA_k and cD_k are wavelet coefficients at the k -th level. Based on (3), DWT can be performed in a cascading process. The black paths in [Fig. 5](#) indicate the process of cascading DWT applied to a signal x .

Reversely, inverse discrete wavelet transform (IDWT) represents the inverse process of DWT [44], and the corresponding operator pair is:

$$\begin{cases} IDWT_A(u) = ((u) \uparrow 2) * LoF^{-1} \\ IDWT_D(u) = ((u) \uparrow 2) * HiF^{-1} \end{cases} \quad (4)$$

where LoF^{-1} and HiF^{-1} are the inverse filters of LoF and HiF , respectively, and \uparrow denotes the upsampling operator. The signal x and its approximation coefficients cA_k at any level can be reconstructed from the IDWT of wavelet coefficients at the next level, as expressed below.

$$\begin{cases} x = IDWT_A(cA_1) + IDWT_D(cD_1) \\ cA_k = IDWT_A(cA_{k+1}) + IDWT_D(cD_{k+1}) \end{cases} \quad k = 1, 2, \dots \quad (5)$$

The cascading reconstruction process of x is shown by the blue paths in [Fig. 5](#). Therefore, when a signal x is decomposed to the n -th level ($n > 1$), it can be exactly reconstructed as follows.

$$x = R_n(cA_n) + \sum_{k=1}^n R_k(cD_k) \quad (6)$$

where $R_n(cA_n)$ is the n -step reconstruction of cA_n and $R_k(cD_k)$ is the k -step reconstruction of cD_k :

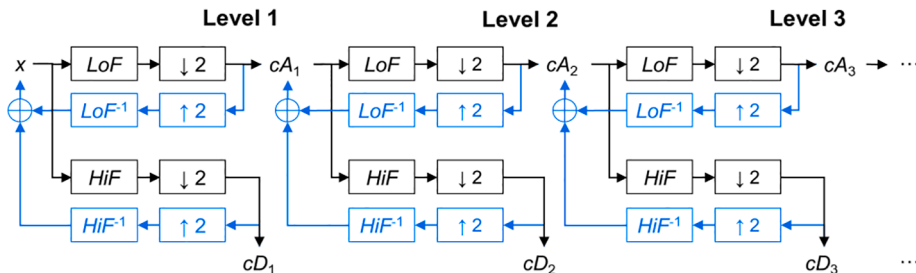


Fig. 5. Block diagram of cascading DWT (black paths) and IDWT (blue paths).

$$\begin{cases} R_n(cA_n) = \text{IDWT}_A^n(cA_n) \\ R_1(cD_1) = \text{IDWT}_D(cD_1) \\ R_k(cD_k) = \text{IDWT}_A^{k-1}[\text{IDWT}_D(cD_k)] \quad k = 2, \dots, n \end{cases} \quad (7)$$

where $\text{IDWT}^k(\cdot)$ represents repeating IDWT k times. Equation (6) shows that a signal can be represented as the superposition of a term related to approximation coefficients and n terms related to detail coefficients, describing the deterministic component and the noise, respectively.

3.1.2. Wavelet-based spike detection

Detail coefficients are sensitive to nonsmooth features in a signal, e.g., jumps and spikes, and have been used to detect spikes or outliers in [30] and [45–47]. Instead of directly using detail coefficients, we propose a new method as follows.

Step A1. Perform n -level DWT of a signal x according to (2) and (3) to obtain a series of detail coefficients cD_1, cD_2, \dots, cD_n .

Step A2. Perform k -step reconstruction of cD_k ($k = 1, \dots, n$) according to (7) to obtain a series of reconstructed signals $R_1(cD_1), R_2(cD_2), \dots, R_n(cD_n)$.

Step A3. Calculate a spike indicator based on the reconstructed signals $R_k(cD_k)$ as follows.

$$R_D = \sum_{k=1}^n |R_k(cD_k)| \quad (8)$$

Step A4. Label the locations at which R_D is greater than a threshold T_1 as spikes.

Using the reconstructed signals $R_k(cD_k)$ to indicate spikes has the following advantages over using the detail coefficients cD_k .

- The detail coefficients are scaling factors of DWT, so detecting spikes based on them requires some prior estimates or assumptions, e.g., in [45] and [46]. In contrast, the reconstructed signals directly represent the amplitude of the noise in a signal.
- Each level of DWT reduces the size of the detail coefficients by half, which needs to be handled when labelling spikes, e.g., in [45] and [46]. In contrast, the reconstructed signals are of the same length as the original signal and do not require special treatment.

3.1.3. Parameter selection

There are three important parameters to select in the proposed method.

Wavelet type. Haar wavelet is recommended because it has shown effectiveness in producing large detail coefficients at locations of outliers [45,46].

Decomposition level n . It determines the depth to which the noise is decomposed. As n increases, the spike indicator R_D increases, getting closer to the spike amplitude, but the temporal resolution of $R_n(cD_n)$ deteriorates. Therefore, we recommend selecting n as follows so that the resolution of $R_n(cD_n)$ is sufficiently higher compared to the average spike duration.

$$n \ll \log_2(\bar{l} \cdot f_s) \quad (9)$$

where \bar{l} is a rough estimate of the average spike duration, and f_s is the sampling frequency.

Threshold T_1 . It can be selected based on the cumulative frequency distribution of R_D above different values, denoted as $P(R_D > R)$. Ideally, as R increases from 0 to infinity, $P(R_D > R)$ decreases from 1 to 0, first sharply and then slowly. The critical point is a good balance between fewer false positives (genuine vibrations are labelled as spikes) and fewer false negatives (spikes are missed), so the value of the critical point can be selected as the threshold T_1 . In the absence of a significant critical point (usually when speckle noise occurs very frequently), T_1 can be set to provide a reasonable proportion of labelled points, e.g., $P(R_D > T_1) \approx 0.5$. This leaves some small-amplitude spikes unlabelled to reduce the amount of imputation in Step 2, and these false negatives can be reduced in Step 3.

3.2. Step 2: Imputation

Step 2 aims to replace the detected spikes with estimates based on nearby unlabelled points. This process is known as imputation in time series and is commonly used to handle missing data or outliers [48,49]. Generally, missing points or outliers occur occasionally [50,51], whereas, in our case, spikes occur more frequently, especially at high speeds. Meanwhile, false positives may occur during spike detection, i.e., genuine vibrations are labelled as spikes, and their original values should not be discarded.

The basic idea of imputation is to build a time series model and make predictions at locations labelled as spikes. A widely-used time series model is the autoregressive integrated moving average (ARIMA) model. For example, in [50], an ARIMA model with exogenous inputs is used for outlier imputation, and in [52], a seasonal ARIMA model is used for missing data imputation. In this section, we use a non-seasonal ARIMA model because the LDVom measurements on large-scale structures do not follow a seasonal pattern.

3.2.1. Training and replacement with an ARIMA model

A non-seasonal ARIMA model is defined as a three-tuple $\text{ARIMA}(p, d, q)$. The autoregressive order p defines the number of past points used to regress the evolving point. The differencing order d defines the times of differencing applied to the original time series.

The moving average order q defines the number of past regression error terms used to regress the evolving error. The ARIMA model for a time series x_t indexed by t is [53]:

$$\left(1 - \sum_{i=1}^p \alpha_i L^i\right) (1 - L)^d x_t = \left(1 + \sum_{j=1}^q \theta_j L^j\right) \varepsilon_t \tag{10}$$

where ε_t is the regression error indexed by t , α_i is the regression coefficient for the i -th autoregressive term ($i = 1, \dots, p$), θ_j is the regression coefficient for the j -th moving average term ($j = 1, \dots, q$), L^i is the i -step lag operator, and $(1-L)^d$ represents the d -th order differencing.

The regression coefficients of an ARIMA model with defined orders can be estimated based on a time series from measurements, known as the training process. Considering the presence of speckle noise, we list three training strategies in Table 2, including their advantages and disadvantages. We will use the direct training strategy in Section 4 ~ 5.

A trained ARIMA model can predict the values of the future points $\hat{x}_{t+1}, \dots, \hat{x}_{t+s}$ based on the past points $x_{t-p-d+1}, \dots, x_t$ through differencing, forecasting, and reversing. For example, the process of one-step ($s = 1$) prediction in the case of $d = 1$ is as follows.

$$\begin{cases} y_t = x_t - Lx_t \\ \hat{y}_{t+1} = \sum_{i=0}^{p-1} \alpha_{i+1} L^i y_t + \sum_{j=0}^{q-1} \theta_{j+1} L^j \varepsilon_t \\ \hat{x}_{t+1} = \hat{y}_{t+1} + x_t \end{cases} \tag{11}$$

As mentioned above, false positives may exist in the time series after spike detection. To reduce the influence of imputation on false positives, we apply the following replacement strategy after making predictions at locations of labelled points.

$$x'_t = \begin{cases} \hat{x}_t & \text{if } |\hat{x}_t - x_t| \geq \lambda \cdot h_{\min} \\ x_t & \text{if } |\hat{x}_t - x_t| < \lambda \cdot h_{\min} \end{cases} \tag{12}$$

where x_t is the original value, \hat{x}_t is the predicted value, λ is a scaling factor, h_{\min} is a rough estimate of the minimum spike amplitude, and x'_t is the point after replacement. This strategy identifies a false positive and trusts its original value when the difference between the predicted and original values is sufficiently small.

3.2.2. Multi-offset and bi-directional imputation

Based on the above fundamentals, we propose the following steps of bi-directional training and replacement to involve data points on both sides of a spike into the imputation process.

- Step B1.** Train a time series model along the forward direction using a strategy in Table 2.
- Step B2.** Make predictions for each segment of labelled points along the forward direction and make replacement according to (12). Use the replaced segments for future predictions.
- Step B3.** Perform Step B1 ~ B2 along the backward direction.
- Step B4.** Average the forward and backward replacement results.

Based on the bi-directional training and replacement process, we further propose a multi-offset imputation method, as shown in Fig. 6. The major steps are as follows.

- Step C1.** Pad the original signal on both ends with $d + p$ points that are equal to the first and the last points, respectively.
- Step C2.** Downsample the padded signal by a factor of r .

Table 2
Different training strategies for imputation.

Strategies	Descriptions	Advantages	Disadvantages
Direct training	<ul style="list-style-type: none"> • Train the model using all data points, including spikes, through a traditional method, e.g., the Box–Jenkins method [53]. 	<ul style="list-style-type: none"> • The most straightforward. 	<ul style="list-style-type: none"> • The participation of spikes may skew the regression coefficients of the model [50].
Training with unlabelled points	<ul style="list-style-type: none"> • Train the model using only unlabelled data through the methods in [54] or [55]. 	<ul style="list-style-type: none"> • Only genuine vibrations (mixed with false negatives) are used for training. 	<ul style="list-style-type: none"> • Loss of information in case of false positives. • Problematic when speckle noise affects most parts of the signal.
Training after manipulation [50,56]	<ul style="list-style-type: none"> • Replace the detected spikes with local means or other statistics. • Train the model using the manipulated signal through a traditional method. 	<ul style="list-style-type: none"> • Maintain the data size for training. • Reduce the disturbance of spikes. 	<ul style="list-style-type: none"> • Manipulation may induce extra dynamics or eliminate important dynamics.

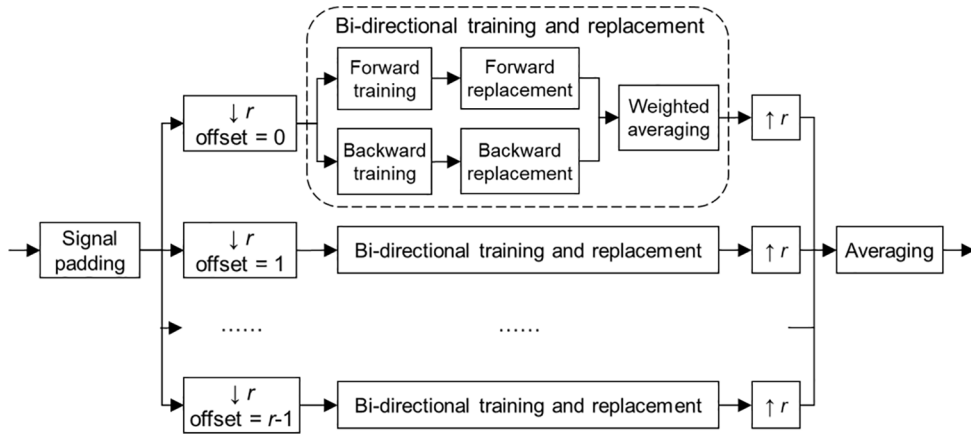


Fig. 6. Flowchart of multi-offset imputation with bi-directional training and replacement.

Step C3. For each downsampled signal with a certain offset, perform bi-directional training and replacement (Steps B1 ~ B4) to produce an imputation result.

Step C4. Upsample each imputation result by the factor of r through interpolation and average all the imputation results with different offsets.

Padding the signal in Step C1 allows the imputation process to cover the entire signal. Downsampling in Step C2 reduces the model order. Using downsampled signals with different offsets in Step C3 ~ C4 can improve the imputation accuracy. Additionally, the proposed imputation method is not only applicable to ARIMA models but also to other time series models.

3.2.3. Parameter selection

There are several parameters to select in the proposed imputation method. First, the ARIMA model orders (d, p, q) need to be selected depending on the choice of the training strategy. For training with unlabelled data or after manipulation, spikes are excluded, so the model orders can be selected through traditional methods, e.g., the autocorrelation function (ACF)-based method [53] and the Akaike information criterion [57]. For the direct training strategy, selecting the model orders is tricky due to the involvement of spikes in the regression process. We propose the following strategy to deal with this situation.

Differencing order d . Appropriate differencing is necessary to treat the nonstationarity caused by spikes. A good choice of d should provide a differenced time series with an ACF that rapidly decays with respect to the lag [53]. Therefore, we recommend increasing d from 1 until the ACF meets this criterion.

Moving average order q . Since the ACF usually turns from positive to negative after differencing, an appropriate q is needed. Meanwhile, q should not be too large so as to limit the influence of regression errors due to spikes, e.g., $q = 1$ can be sufficient.

Autoregressive order p . It should be selected properly to capture the dynamics of genuine vibrations. We recommend initially setting p based on the average spike duration \bar{l} as follows and then adjusting it by evaluating the imputation performance.

$$p = \frac{\bar{l} \cdot f_s}{r} \tag{13}$$

Downsampling is recommended in Step C2 when the sampling frequency f_s is high enough. According to (13), a larger downsampling factor r can reduce the autoregressive order p of the ARIMA model, thereby reducing the computational cost. Meanwhile, the integer r should be restricted so that f_s/r is sufficiently higher than the highest frequency of interest.

The scaling factor λ in (12) determines the boundary between trusting the original point and the predicted value. It should be set to a small value, e.g., at least below 0.2, so that false positives are recovered but not real spikes. In this case, the imputation performance is not sensitive to λ , since only predicted points with small deviations from the original points are affected.

Finally, for each segment of labelled points, we recommend predicting additional c points ahead in both directions in Step B2 and calculating the weighted average of the bi-directional results in Step B4 based on the following weighting functions.

$$w_f(x) = \begin{cases} \frac{-2|e_f|}{|e_f| + |e_b|} \frac{x}{l} + 1 & 0 \leq x < \frac{l}{2} \\ \frac{-2|e_b|}{|e_f| + |e_b|} \left(\frac{x}{l} - 1\right) & \frac{l}{2} \leq x \leq l \end{cases} \quad w_b(x) = \begin{cases} \frac{2|e_f|}{|e_f| + |e_b|} \frac{x}{l} & 0 \leq x < \frac{l}{2} \\ \frac{2|e_b|}{|e_f| + |e_b|} \frac{x}{l} + \frac{|e_f| - |e_b|}{|e_f| + |e_b|} & \frac{l}{2} \leq x \leq l \end{cases} \tag{14}$$

where l is the length of labelled points, $w_f(x)$ (or $w_b(x)$) is the weight for the forward (or backward) replacement result at position x , and e_f (or e_b) is the forward (or backward) terminal error, i.e., the average prediction error for the additional c points. The parameter c can

be set to a small integer, such as 3 ~ 5. The above averaging strategy is illustrated in Fig. 7, in which both the distance to the boundary and the terminal error contribute to the determination of weights. The following properties hold for the weighting functions in (14).

- $w_f(x) + w_b(x) = 1$; $w_f(0) = 1$; $w_b(l) = 1$.
- $w_f(x)$ is a decreasing function of x , and $w_b(x)$ is an increasing function of x .
- If $|e_f|/|e_b|$ decreases, $w_f(x)$ will increase and $w_b(x)$ will decrease, and vice versa.
- At the midpoint ($x = l/2$), the weights depend only on the terminal errors:

$$w_f\left(\frac{l}{2}\right) = \frac{|e_b|}{|e_f| + |e_b|} \quad w_b\left(\frac{l}{2}\right) = \frac{|e_f|}{|e_f| + |e_b|} \tag{15}$$

3.3. Step 3: smoothing

The signal processed after Step 1 and Step 2 may still contain undesired noise, such as false negatives in spike detection that remain untreated, errors induced in the imputation process, and abrupt changes due to switching between the two options in (12).

Step 3 aims to reduce the residual noise while preserving the genuine vibration. It is implemented by applying a classical smoothing or denoising method because the residual noise is no longer as broadband as the raw speckle noise. In this paper, we use a Butterworth filter. For example, the gain of an m -order low-pass Butterworth filter is [58]:

$$G^2(\omega) = \frac{G_0^2}{1 + \left(\frac{j\omega}{j\omega_c}\right)^{2m}} \tag{16}$$

where G_0 is the gain at zero frequency and ω_c is the cut-off frequency. It shows that the amplitude-frequency response of a Butterworth filter is monotonic, being maximally flat in the passband while rolling off towards zero in the stopband [59]. Since the residual noise is less broadband, the cut-off frequency can be set equal to the highest frequency of interest.

Fig. 8 illustrates the signal flow in the proposed despeckle framework. Spikes are detected at Step 1 and replaced at Step 2. False positives are recovered at Step 2. False negatives and residual noise are smoothed at Step 3. A significant advantage of the proposed despeckle framework is that other different methods can be adapted and used at different steps. Some potential options from our literature survey are discussed in Appendix.

4. Stepwise validation

In this section, the proposed despeckle framework is validated following a stepwise process.

4.1. Validation of Step 1

Taking the signal in Fig. 4(a) as an example, we show the reconstructed signal $R_k(cD_k)$ at different level k in Fig. 9(a), where as k increases, the temporal resolution of $R_k(cD_k)$ deteriorates, while its size remains the same as the original signal. Further, we show the

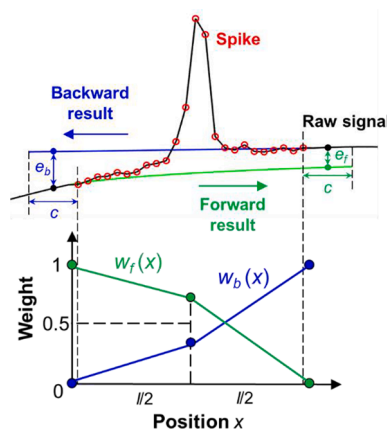


Fig. 7. Weighting functions.

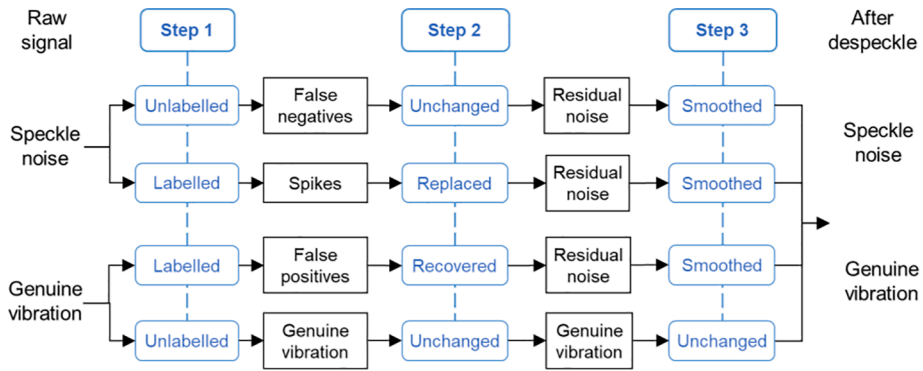


Fig. 8. Signal flow in the three-step despeckle framework.

spike indicator R_D for different n in Fig. 9(b), where as n increases, R_D gets larger at the locations of spikes, and the amplitude of R_D is correlated with the corresponding spike amplitude.

According to (9), the decomposition level of $n = 3$ is selected. Then, the cumulative frequency distribution of R_D is plotted in Fig. 10 (0.5 km/h). A critical point can be observed, so the threshold of $T_1 = 0.1$ mm/s is selected. The corresponding detection result in Fig. 9 (c) shows that all the manually selected spikes in Fig. 4(a) are automatically detected.

Similarly, Figs. 10 and 11 show the spike detection results for the two samples in Fig. 4(b)~(c), respectively. For the higher speeds, the selected n is smaller due to the shorter spike duration, and the selected T_1 is larger due to the larger spike amplitude. It is noteworthy that in Fig. 10 no critical point is observed at 20 km/h, so we select $T_1 = 2$ mm/s to label approximately half of the points as spikes. Compared with the manual selection in Fig. 4, most of the spikes are detected. Meanwhile, some false positives and false negatives can be observed, e.g., the points labelled in Fig. 9(c) and Fig. 11(c)~(d). They will be addressed through the replacement strategy at Step 2 and the smoothing method at Step 3, respectively.

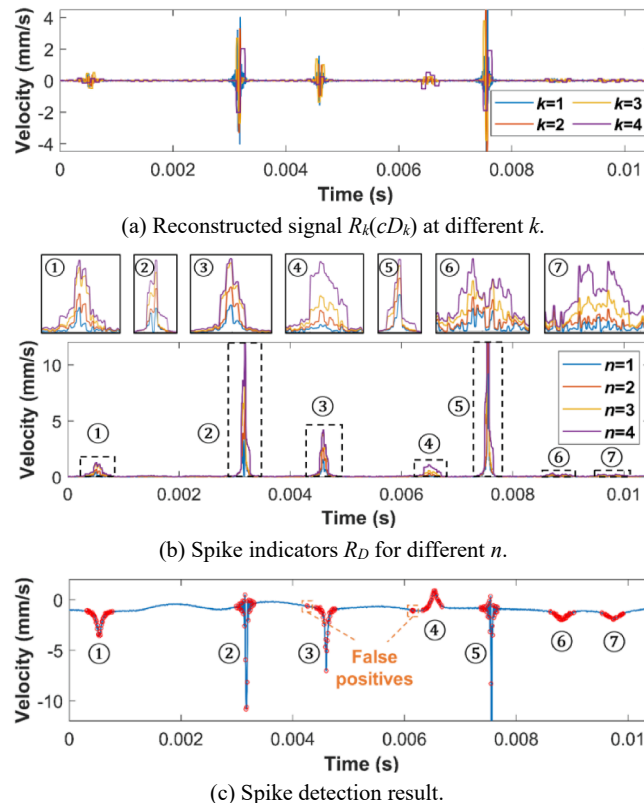


Fig. 9. Wavelet-based spike detection at 0.5 km/h.

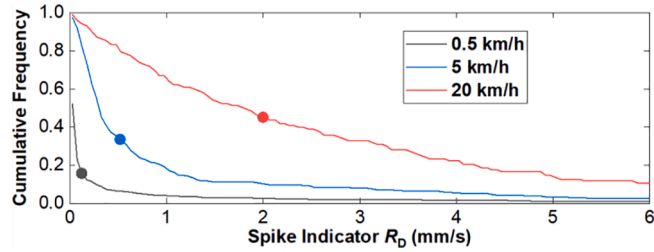


Fig. 10. Cumulative frequency of spike indicators R_D at different speeds.

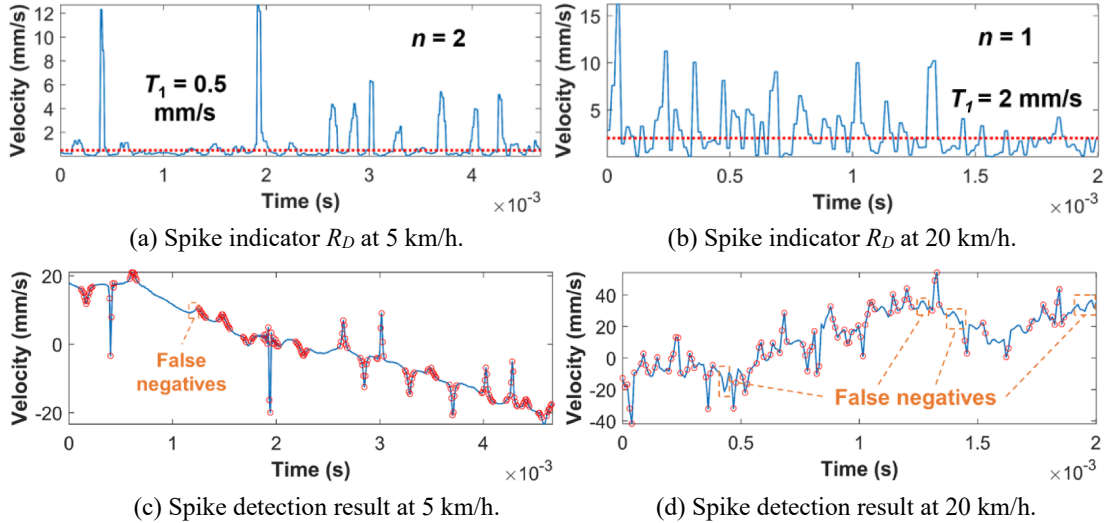


Fig. 11. Wavelet-based spike detection at 5 km/h and 20 km/h.

4.2. Validation of Step 2

In our case study, we use the strategy of direct training in Table 2 for imputation. To showcase the design of ARIMA models following Section 3.2.3, we take the above three samples as examples and show their ACFs at different differencing orders d in Fig. 12. The plots for $d = 0$ show slow-decay patterns, the plots for $d = 1$ show rapid-decay patterns, and the plots for $d = 2$ indicate over-differencing. Meanwhile, the ACFs turn from positive to negative after differencing. Therefore, we select $d = 1$ and $q = 1$ for all the three samples.

Since speckle noise masks genuine vibrations in real signals, we propose a Monte Carlo-based strategy to create artificial noisy signals by superposing the collected spike samples with base signals free of speckle noise (from non-LDV measurements or simulations). At each time instant of a base signal, a random number between 0 and 1 is generated. Once it is smaller than a defined scalar p_s , a spike sample is randomly selected, and its amplitude is scaled by a factor a_s . Then, the left and right halves of the spike sample are scaled separately and superposed with the base signal with smooth transitions. Afterwards, imputation is performed for the artificial signal at the locations of spikes, and the imputation error is quantified through comparisons with the base signal, as shown in Fig. 13. Additionally, the spike occurrence rate and amplitude are adjustable by changing p_s and a_s , respectively, which allows us to evaluate the imputation accuracy under different speckle noise severity.

Following the above strategy, three artificial signals with different speckle noise severity are generated. Table 3 and Table 4 compare the imputation performance between different ARIMA model orders, including the mean square error (MSE) at all spike locations and the total CPU time (on Intel Xeon E5-2643 @3.30 GHz). The influence of p is small in a certain range ($p = 20 \sim 50$) but becomes significant when it is too large or too small. It shows that $d = 1, q = 1, p = 40$ outperforms the other choices in terms of imputation errors, demonstrating the effectiveness of the model order selection strategy in Section 3.2.3.

Table 5 compares the imputation performance under different downsampling strategies, in which p is adjusted with respect to the downsampling factor r according to (13). A higher r significantly reduces the computational cost, and averaging the imputation results from multiple offsets slightly improves the imputation accuracy over using only one offset.

Table 6 compares the imputation accuracy under different averaging strategies in the bi-directional training and replacement process. Compared to the other strategies, the proposed weighted averaging strategy reduces the imputation error significantly.

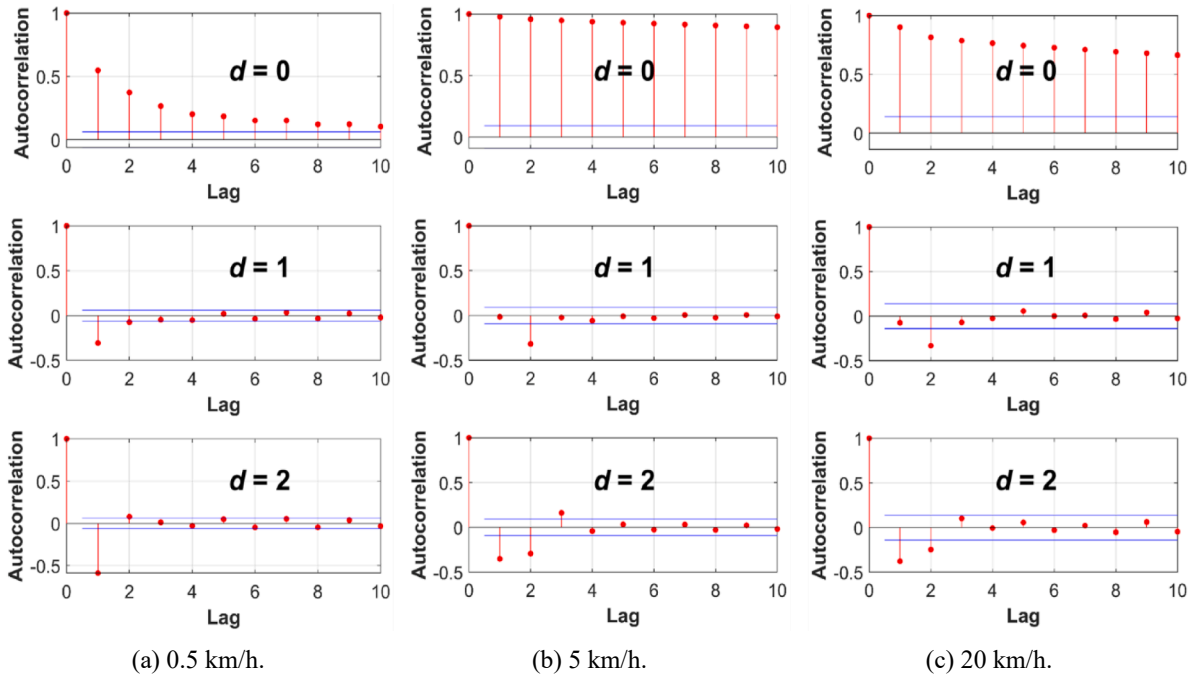


Fig. 12. ACF plots for different d .

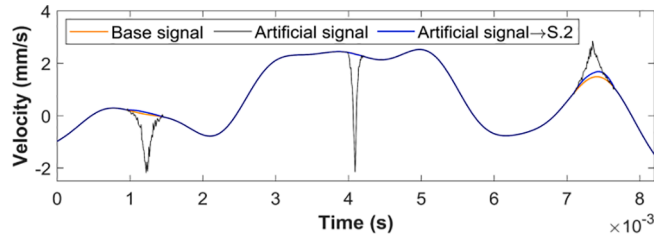


Fig. 13. An imputation example based on an artificial signal. ‘Artificial signal \rightarrow S.2’ represents applying Step 2 alone to the artificial signal.

Table 3

Imputation performance under different d and q .

ARIMA models			Artificial signal 1 $p_s = 0.002, a_s = 1$		Artificial signal 2 $p_s = 0.004, a_s = 1$		Artificial signal 3 $p_s = 0.004, a_s = 2$	
p	d	q	MSE (mm/s)	CPU time (s)	MSE (mm/s)	CPU time (s)	MSE (mm/s)	CPU time (s)
$p = 40$ (according to (13))	$d = 0$	$q = 1$ (according to Fig. 12)	0.010537	81.843	0.004112	79.97	0.004225	79.11
		$d = 2$	0.002198	101.84	0.002133	110.41	0.001667	107.94
	$d = 1$ (according to Fig. 12)	$q = 0$	0.001373	88.67	0.001571	88.03	0.001240	89.08
			0.004033	72.11	0.003596	103.88	0.004343	60.44
		$q = 2$	0.001390	89.31	0.001572	97.27	0.001336	91.16

4.3. Validation of Step 3

In this section, we use real signals to validate the despeckle framework. First, three samples measured at 0.5 km/h are shown in Fig. 14. For each sample, the upper plot compares the raw signal with the product of the first two steps, while the lower plot compares the final despeckle outcome with the result of applying the filter in Step 3 alone to the raw signal. We adopt a low-pass filter with $\omega_c = 3$ kHz in Step 3, considering the track vibration is generally below 3 kHz. It shows that the speckle noise is effectively eliminated by detecting and replacing the spikes, whereas the direct use of the low-pass filter leaves significant residual noise because the speckle noise at 0.5 km/h contains components below 3 kHz, as shown in Fig. 4(a).

Table 4
Imputation performance under different p .

ARIMA models			Artificial signal 1		Artificial signal 2		Artificial signal 3	
p	d	q	MSE (mm/s)	CPU time (s)	MSE (mm/s)	CPU time (s)	MSE (mm/s)	CPU time (s)
$p = 0$	$d = 1$ (according to Fig. 12)	$q = 1$ (according to Fig. 12)	0.002581	3.23	0.002187	6.52	0.002065	5.36
$p = 5$			0.002699	8.03	0.002145	11.05	0.001886	9.95
$p = 10$			0.002812	11.45	0.002128	16.11	0.001846	16.80
$p = 20$			0.001257	35.11	0.002136	33.69	0.001748	34.73
$p = 30$			0.001297	52.27	0.002056	55.27	0.001579	56.39
$p = 40$ (according to (13))			0.001373	88.67	0.001571	88.03	0.001240	89.08
$p = 50$			0.002009	114.97	0.001636	130.31	0.001278	118.16
$p = 60$			0.004671	148.22	0.002460	155.94	0.004929	160.08
$p = 70$			0.004438	265.78	0.003492	289.16	0.004598	287.84

Table 5
Imputation performance under different downsampling strategies.

Downsampling strategies			Artificial signal 1		Artificial signal 2		Artificial signal 3	
r	p	Offset	MSE (mm/s)	CPU time (s)	MSE (mm/s)	CPU time (s)	MSE (mm/s)	CPU time (s)
$r = 1$	$p = 40$	/	0.001373	88.67	0.001571	88.03	0.001240	89.08
$r = 2$	$p = 20$	Single offset	0.001434	24.80	0.001656	29.90	0.001593	28.90
		Multiple offsets	0.001429	49.59	0.001643	59.80	0.001243	57.80
$r = 3$	$p = 14$	Single offset	0.001425	15.23	0.001672	18.51	0.001359	17.70
		Multiple offsets	0.001423	45.69	0.001657	55.53	0.001347	53.11

Table 6
Imputation performance under different averaging strategies.

Averaging strategies	MSE (mm/s)		
	Artificial signal 1	Artificial signal 2	Artificial signal 3
Only forward replacement	0.006353	0.005300	0.005774
Only backward replacement	0.005937	0.005342	0.005797
Direct average	0.003723	0.003276	0.003307
Weighted average (according to Section 3.2.3)	0.001373	0.001571	0.001240

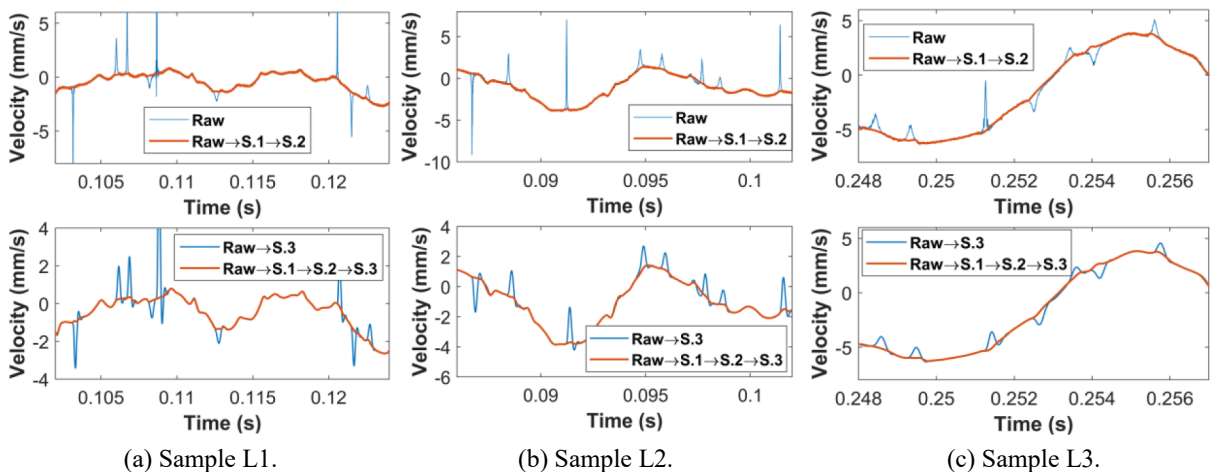


Fig. 14. Despeckle samples at 0.5 km/h. ‘Raw’ represents the raw signal, ‘Raw → S.1 → S.2’ represents the product of the first two steps, ‘Raw → S.1 → S.2 → S.3’ represents the final despeckle outcome, ‘Raw → S.3’ represents applying Step 3 alone to the raw signal.

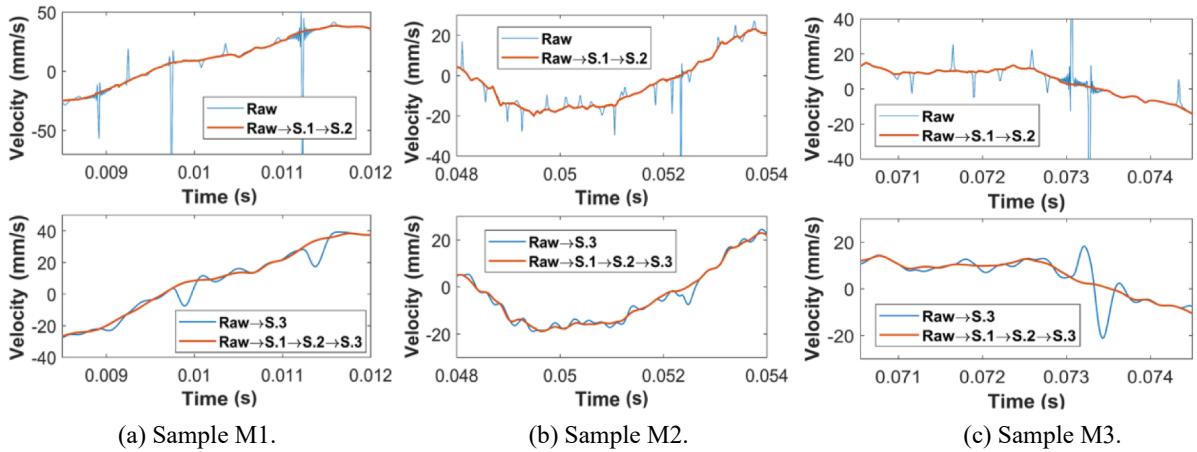


Fig. 15. Despeckle samples at 5 km/h.

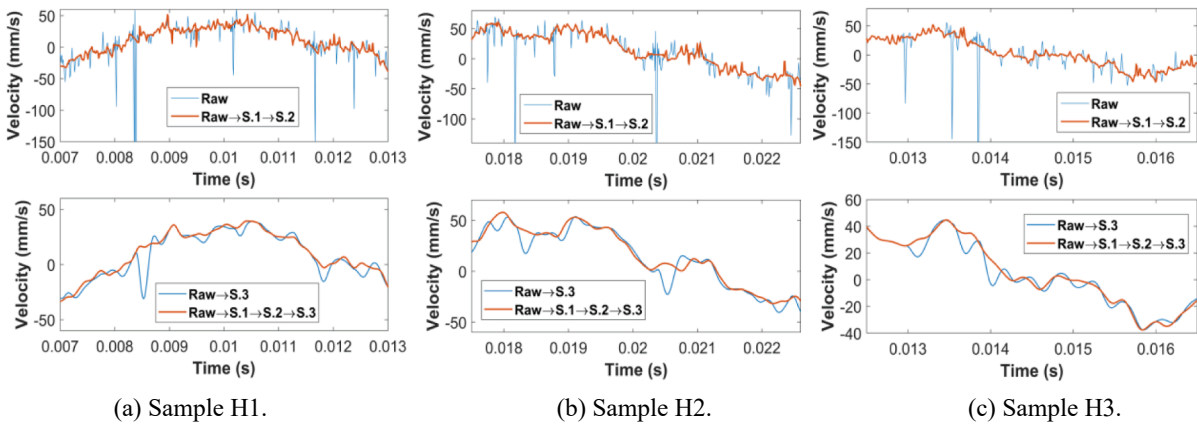


Fig. 16. Despeckle samples at 20 km/h.

Similarly, Fig. 15 shows three despeckle samples at 5 km/h. Compared to Fig. 14, the residual noise after direct filtering becomes lighter since the speckle noise at 5 km/h has a higher frequency band, according to Fig. 4(b). However, as the sharpness of spikes is reduced, the residual noise looks more like vibrations. This pseudo vibration is not a real structural response but the low-frequency part of the speckle noise due to insufficient despeckle. The proposed three-step framework can effectively avoid this problem.

The despeckle performance for signals measured at 20 km/h is shown in Fig. 16. Since the speckle noise affects most parts of the signals, the despeckle framework allows some false negatives (small-amplitude spikes) in Step 1 so as to reduce the amount of imputation in Step 2. Then, the residual noise is filtered out in Step 3. In this way, the proposed three-step framework effectively reduces speckle noise while avoiding pseudo vibrations.

5. Comparison with trackside measurements

To verify the LDVom measurements, we mount two accelerometers (PCB 356B21) near the laser spot trajectory on one sleeper and one segment of the track slab, as shown in Fig. 17. The trackside measurements are performed under the same condition as the LDVom measurements. Among the different speeds, we only analyse 20 km/h because its speckle noise is the most severe. Besides, to enable comparisons in the same unit, we convert the measured accelerations to velocities through frequency-domain integration [60].

First, the track vibration excited by passing the joint in Segment A is analysed. Fig. 18(a) shows the raw LDVom signals at two laps, and the upper plot in Fig. 18(b) shows the corresponding despeckle results using the proposed methods (a 150 ~ 3,000 Hz band-pass filter is adopted in Step 3), which reflects good repeatability between the two laps. The bottom plot in Fig. 18(b) shows the averaged trackside measurements for two laps. The LDVom measurements after despeckle have good agreement with the trackside measurements. The dominant component at around 500 Hz is measured, and some high-frequency behaviour related to sleeper dynamics is captured. The amplitudes of trackside measurements are lower than the LDVom measurements because the accelerometers are located at a distance from the joint. In addition, given the fact that the laser irradiates sleepers and track slabs in turn as the platform moves, we find that the proposed method is effective for the measurements on both surfaces.

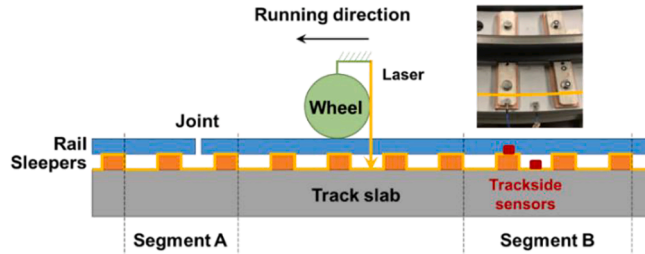
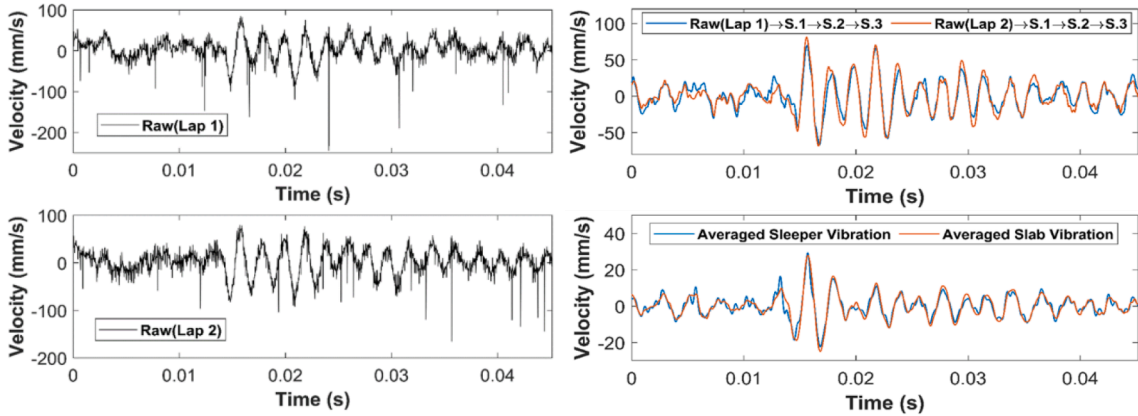


Fig. 17. Setup of trackside vibration measurements.



(a) Raw LDV signals at different laps.

(b) Despeckle results and trackside signals.

Fig. 18. Comparison with trackside measurements (Segment A).

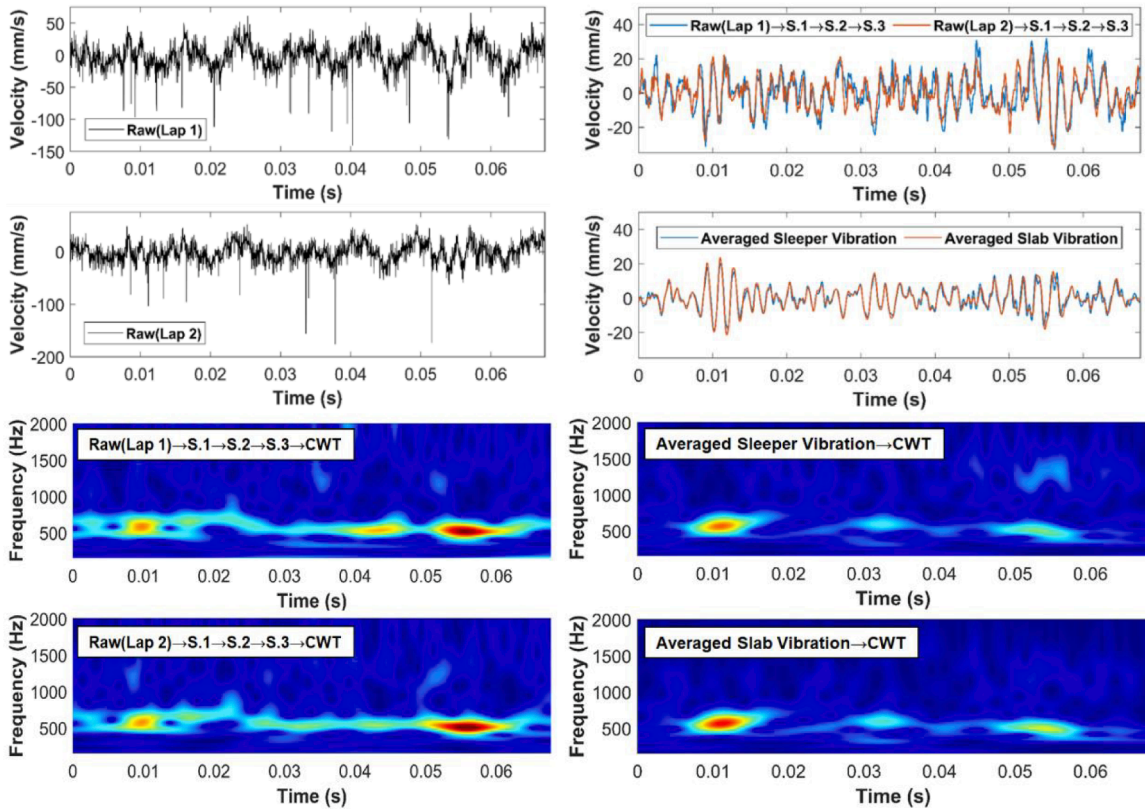
Then, the measurement results on the normal track in Segment B are shown in Fig. 19, including their time–frequency characteristics (at the same scale) after CWT with Morlet wavelet [43]. Compared with the trackside measurements, the LDVom successfully captures the dominant track vibration at 500 ~ 700 Hz, and their amplitudes are similar. The repeatability and agreement are not as good as those in Fig. 18 due to the lower signal-to-noise ratio and the random nature of wheel-track dynamics.

Finally, the computational cost of the proposed methods is evaluated. In our case study, passing each sleeper segment at 20 km/h takes approximately 22.6 ms, while the corresponding CPU time for despeckle is 17.5 s on average. Although the despeckle algorithm cannot be implemented in real-time, it can be applied offline at acceptable computational costs.

6. Conclusions

In this paper, we study the characteristics of the speckle noise from LDVom measurements on railway tracks, propose and validate a three-step framework for speckle noise reduction, and compare the LDVom measurements with the trackside measurements. Specifically, we develop a wavelet-based spike detection method at Step 1 and an ARIMA-based imputation method at Step 2, and adopt a Butterworth filter at Step 3. The main conclusions are summarised below.

- 1) In the time domain, the spikes occur discretely with random amplitudes and durations. In the frequency domain, they are broadband and can overlap with genuine vibrations. As the moving speed increases, the speckle noise occurs more frequently with shorter durations, greater amplitudes, and broader frequency bands.
- 2) When applying conventional methods to despeckle, the amplitude of spikes can be shortened but not eliminated, which can lead to pseudo vibrations. The three-step framework can avoid this problem by detecting and replacing spikes, recovering false positives, and smoothing false negatives and residual noise.
- 3) In addition to the proposed methods, different alternative methods can be adapted and used in the three steps of the despeckle framework. In Step 2, different training strategies can be selected considering the presence of speckle noise in time series.
- 4) The proposed methods can effectively reduce the speckle noise at different speeds, among which the highest speed in this paper is 20 km/h. The computational cost of the proposed methods is acceptable for offline applications.
- 5) In our case study, the LDVom measurements can successfully capture the dominant components of the track vibrations at around 500 ~ 700 Hz with good repeatability between different laps and good agreement with trackside measurements.



(a) Raw LDV signals at different laps. (b) Despeckle results and trackside signals.

Fig. 19. Comparison with trackside measurements (Segment B).

For future research, we will closely monitor state-of-the-art LDV technologies and investigate their performance in LDVom applications. We will also develop adaptive methods to automatically determine the optimal parameters for spike detection and imputation. Furthermore, a complete comparison between different methods at different steps based on a benchmark is highly desirable.

Funding

This work was partly supported by the Dutch Topconsortium voor Kennis en Innovatie, HighTech Systemen & Materialen program [reference number TKI HTSM/19.0172] and ProRail.

Declaration of Competing Interest

The authors declare that they have no known competing financial interests or personal relationships that could have appeared to influence the work reported in this paper.

Acknowledgement

The authors would like to express special thanks to Jan Moraal for his contribution to the measurements in the laboratory.

Appendix

In the proposed despeckle framework, we use a wavelet-based method for Step 1, an ARIMA-based method for Step 2, and a Butterworth filter for Step 3. A significant advantage of the proposed framework is that other different methods can also be adapted and used at different steps. Table A lists some other alternative methods from our literature survey. This table is intended to provide some potential options for each step and discuss their pros and cons.

Table A1
Different options at the three steps.

Step 1: Spike detection			
Methods	Descriptions	Advantages	Disadvantages
Wavelet-based (Section 3.1)	<ul style="list-style-type: none"> Calculate a spike indicator through wavelet decomposition and reconstruction. 	<ul style="list-style-type: none"> The spike indicator reflects the noise amplitude. 	<ul style="list-style-type: none"> Require multi-level DWT and IDWT.
Wavelet-based [30,45,46]	<ul style="list-style-type: none"> Calculate the detail coefficients through wavelet decomposition. 	<ul style="list-style-type: none"> No IDWT required. 	<ul style="list-style-type: none"> Thresholding requires prior estimates or assumptions. Size reduction due to downsampling. Frequency-dependent time delay.
High-pass filter-based [30]	<ul style="list-style-type: none"> Filter the raw signal by a high-pass filter. 	<ul style="list-style-type: none"> Easy to implement in frequency domain. 	
Local statistics-based [5,9,35]	<ul style="list-style-type: none"> Calculate the local variance/kurtosis in a sliding window. 	<ul style="list-style-type: none"> Easy to implement in time domain. 	<ul style="list-style-type: none"> Spike boundaries are difficult to determine.
Short-time energy-based [9]	<ul style="list-style-type: none"> Calculate the average short-time energy in a sliding window. 	<ul style="list-style-type: none"> Sensitive to spikes of long duration. 	<ul style="list-style-type: none"> Spike boundaries are difficult to determine.
Residual-based [50]	<ul style="list-style-type: none"> Build a time series model for the raw signal. Calculate residuals to indicate outliers. 	<ul style="list-style-type: none"> Independent of frequency characteristics. 	<ul style="list-style-type: none"> Outliers degrade the regression performance.
Step 2: Imputation			
Methods	Descriptions	Advantages	Disadvantages
ARIMA-based (Section 3.2)	<ul style="list-style-type: none"> Model the time series by ARIMA models. Replace spikes through multi-offset and bi-directional imputation. 	<ul style="list-style-type: none"> Fitting an ARIMA model is deterministic and fast. 	<ul style="list-style-type: none"> Only linear dynamics is captured. Spikes degrade the training performance.
ARIMA-based [50]	<ul style="list-style-type: none"> Outliers are replaced by local means. Model the manipulated time series by an ARIMA model and make predictions. 	<ul style="list-style-type: none"> Fitting an ARIMA model is deterministic and fast. The disturbance of outliers is reduced. 	<ul style="list-style-type: none"> Only linear dynamics is captured. Manipulation may induce extra dynamics or eliminate important dynamics.
Linear prediction-based [9,35]	<ul style="list-style-type: none"> Model the time series by a linear prediction model. Replace spikes through linear prediction. 	<ul style="list-style-type: none"> Fitting a linear prediction model is fast. 	<ul style="list-style-type: none"> Only linear dynamics is captured.
Support vector machine (SVM)-based [56]	<ul style="list-style-type: none"> Replace outliers or missing values with temporal information. Model the time series by an SVM and make predictions. 	<ul style="list-style-type: none"> Capture nonlinear dynamics by a kernel method. The disturbance of outliers is reduced. 	<ul style="list-style-type: none"> Non-explicit interpretability. Manipulation may induce extra dynamics or eliminate important dynamics.
Artificial neural network (ANN)-based [61]	<ul style="list-style-type: none"> Model the time series by an ANN and make predictions. Optimisation is usually required to improve accuracy. 	<ul style="list-style-type: none"> Capture nonlinear dynamics. 	<ul style="list-style-type: none"> Computationally demanding. Non-explicit interpretability.
Kalman filter-based [51,62]	<ul style="list-style-type: none"> Model the signal by a Kalman filter and make predictions. 	<ul style="list-style-type: none"> Capture dynamic trends. 	<ul style="list-style-type: none"> Sensitive to model design.
Interpolation-based [30,63]	<ul style="list-style-type: none"> Interpolate based on adjacent points. 	<ul style="list-style-type: none"> No modelling required. 	<ul style="list-style-type: none"> Difficult to capture dynamic behaviours.
Step 3: Smoothing			
Methods	Descriptions	Advantages	Disadvantages
Low/band-pass filter (Section 3.3)	<ul style="list-style-type: none"> Filter the signal by a low/band-pass filter. 	<ul style="list-style-type: none"> Clear physical meaning. Preserve genuine vibrations. 	<ul style="list-style-type: none"> Sensitive to the cut-off frequency. Frequency-dependent time delay.
Mean filter [64]	<ul style="list-style-type: none"> Calculate the weighted average in a sliding window. 	<ul style="list-style-type: none"> Easy to implement in time domain. 	<ul style="list-style-type: none"> Reduce genuine vibrations.
Median filter [65,66]	<ul style="list-style-type: none"> Calculate the local median in a sliding window. 	<ul style="list-style-type: none"> Easy to implement in time domain. 	<ul style="list-style-type: none"> Reduce genuine vibrations.
Lee filter [67]	<ul style="list-style-type: none"> Calculate local statistics in a sliding window. 	<ul style="list-style-type: none"> Balance between original values and local statistics. 	<ul style="list-style-type: none"> Reduce genuine vibrations.
Sigma filter [68]	<ul style="list-style-type: none"> Calculate the local mean within a certain deviation. 	<ul style="list-style-type: none"> Exclude outliers. Easy to implement in time domain. 	<ul style="list-style-type: none"> Sensitive to window design. Reduce genuine vibrations.
Wavelet denoise [36,69,70]	<ul style="list-style-type: none"> Perform wavelet transform. Filter out large wavelet coefficients. Reconstruct the signal. 	<ul style="list-style-type: none"> Suitable for nonstationary changes. 	<ul style="list-style-type: none"> Sensitive to wavelet type and decomposition level.

References

- [1] P. Castellini, M. Martarelli, E.P. Tomasini, Laser doppler vibrometry: development of advanced solutions answering to technology's needs, *Mech. Syst. Sig. Process.* 20 (6) (2006) 1265–1285.
- [2] P. Lutzmann, B. Göhler, F. Van Putten, et al., Laser vibration sensing: overview and applications. *Electro-Optical Remote Sensing, Photon. Technol. Appl. V 8186* (2011), 818602.
- [3] S.J. Rothberg, M.S. Allen, P. Castellini, et al., An international review of laser Doppler vibrometry: Making light work of vibration measurement, *Opt. Lasers Eng.* 99 (2017) 11–22.
- [4] M. Gasparetti, G.M. Revel, The influence of operating conditions on the accuracy of in-plane laser Doppler velocimetry measurements, *Measurement* 26 (3) (1999) 207–220.
- [5] J. Vass, R. Šmíd, R.B. Randall, et al., Avoidance of speckle noise in laser vibrometry by the use of kurtosis ratio: application to mechanical fault diagnostics, *Mech. Syst. Sig. Process.* 22 (3) (2008) 647–671.
- [6] M. Muramatsu, S. Uchida, Y. Takahashi, Noncontact detection of concrete flaws by neural network classification of laser doppler vibrometer signals, *Eng. Res. Express.* 2 (2) (2020), 025017.
- [7] P. Garg, F. Moreu, A. Ozdagli, et al., Noncontact dynamic displacement measurement of structures using a moving laser Doppler vibrometer, *J. Bridge Eng.* 24 (9) (2019), 04019089.T1.
- [8] P. Castellini, R. Montanini, Automotive components vibration measurements by tracking laser Doppler vibrometry: advances in signal processing, *Meas. Sci. Technol.* 13 (8) (2002) 1266.
- [9] Y. Wang, W. Zhang, Z. Wu, et al., Speckle noise detection and removal for laser speech measurement systems, *Appl. Sci.* 11 (21) (2021) 9870.
- [10] J. R. D. F. Arruda, S. A. Vianna do Rio, L. A. S. 1996. Bernardes Santos. A space-frequency data compression method for spatially dense laser doppler vibrometer measurements. *Shock Vibration.* 3(2), 127-133.
- [11] D.M. Siringoringo, Y. Fujino, Experimental study of laser Doppler vibrometer and ambient vibration for vibration-based damage detection, *Eng. Struct.* 28 (13) (2006) 1803–1815.
- [12] G.M. Revel, P. Castellini, P. Chiariotti, et al., Laser vibrometry vibration measurements on vehicle cabins in running conditions: helicopter mock-up application, *Opt. Eng.* 50 (10) (2011), 101502.
- [13] C. Rembe, A. Dräbenstedt, Speckle-insensitive laser-Doppler vibrometry with adaptive optics and signal diversity, *Proceedings Sensor.* 2015 (2015) 505–510.
- [14] N. Zandt, M. Spencer, Improved adaptive-optics performance using polychromatic speckle mitigation, *Appl. Opt.* 59 (4) (2020) 1071–1081.
- [15] J. Zhu, Y. Li, R. Baets, Mitigation of speckle noise in laser Doppler vibrometry by using a scanning average method, *Opt. Lett.* 44 (7) (2019) 1860–1863.
- [16] A. Dräbenstedt, Diversity combining in laser Doppler vibrometry for improved signal reliability, in *AIP Conf. Proceed.* 1600 (1) (2014) 263–273.
- [17] S. Courville, P. Sava, Speckle noise attenuation in orbital laser vibrometer seismology, *Acta Astronaut.* 172 (2020) 16–32.
- [18] M. Schewe, C. Rembe, Signal diversity for laser-Doppler vibrometers with raw-signal combination, *Sensors.* 21 (3) (2021) 998.
- [19] M. Schewe, C. Rembe. 2021. Analyzing real-time capability of raw laser-Doppler vibrometer signal combination for signal diversity. In *Optical Measurement Systems for Industrial Inspection XII 11782, 117820E*.
- [20] D. Oliver, V. Palan, G. Bissinger, et al., 3-dimensional laser doppler vibration analysis of a stradivarius violin. In *Proc. 25th International Modal Analysis Conference*, 2007.
- [21] K. Kaynardag, G. Battaglia, A. Ebrahimkhanlou, et al., Identification of bending modes of vibration in rails by a laser Doppler vibrometer on a moving platform, *Exp. Tech.* 45 (1) (2020) 13–24.
- [22] M. Martarelli, D.J. Ewins, Continuous scanning laser Doppler vibrometry and speckle noise occurrence, *Mech. Syst. Sig. Process.* 20 (8) (2006) 2277–2289.
- [23] D. Di Maio, P. Castellini, M. Martarelli, et al., Continuous Scanning Laser Vibrometry: A raison d'être and applications to vibration measurements, *Mech. Syst. Sig. Process.* 156 (2021), 107573.
- [24] A.B. Stanbridge, M. Martarelli, D.J. Ewins, Measuring area vibration mode shapes with a continuous-scan LDV, *Measurement* 35 (2) (2004) 181–189.
- [25] M.S. Allen, M.W. Sracic, A new method for processing impact excited continuous-scan laser Doppler vibrometer measurements, *Mech. Syst. Sig. Process.* 24 (3) (2010) 721–735.
- [26] D.M. Chen, Y.F. Xu, W.D. Zhu, Damage identification of beams using a continuously scanning laser Doppler vibrometer system, *J. Vib. Acoust.* 138 (5) (2016), 051011.
- [27] Y.F. Xu, D.M. Chen, W.D. Zhu, Damage identification of beam structures using free response shapes obtained by use of a continuously scanning laser Doppler vibrometer system, *Mech. Syst. Sig. Process.* 92 (2017) 226–247.
- [28] Y.F. Xu, D.M. Chen, W.D. Zhu, Operational modal analysis using lifted continuously scanning laser Doppler vibrometer measurements and its application to baseline-free structural damage identification, *J. Vib. Control* 25 (7) (2019) 1341–1364.
- [29] M.W. Sracic, M.S. Allen, Experimental investigation of the effect of speckle noise on continuous scan laser Doppler vibrometer measurements. In *27th International Modal Analysis Conference*, 2009.
- [30] V. Aranchuk, A. K. Lal, C. F. Hess, et al. 2006. Speckle noise in a continuously scanning multibeam laser Doppler vibrometer for acoustic landmine detection. In *Detection and Remediation Technologies for Mines and Minelike Targets XI.* 6217, 621716.
- [31] E.J. OBrien, A. Malekjafarian, A mode shape-based damage detection approach using laser measurement from a vehicle crossing a simply supported bridge, *Struct. Contr. Health Monitor.* 23 (10) (2016) 1273–1286.
- [32] B. Libbey, D. Fenneman, B. Burns. Mobile platform for acoustic mine detection applications. *Detection and Remediation Technologies for Mines and Minelike Targets X.* 2005. 5794, 683-693.
- [33] L.A. Jiang, M.A. Albota, R.W. Haupt, et al., Laser vibrometry from a moving ground vehicle, *Appl. Opt.* 50 (15) (2011) 2263–2273.
- [34] S. Rahimi, Z. Li, R. Dollevoet, Measuring with laser Doppler vibrometer on moving frame (LDVMF), *AIP Conf. Proc.* 1600 (1) (2014) 274–286.
- [35] T. Lv, X. Han, S. Wu, et al., The effect of speckles noise on the Laser Doppler Vibrometry for remote speech detection, *Opt. Commun.* 440 (2019) 117–125.
- [36] Y. Jin, Z. Li, Eliminating speckle noises for laser Doppler vibrometer based on empirical wavelet transform, in: *13th International Conference on Measurement*, 2021, pp. 1–4.
- [37] V. Bianco, P. Memmolo, M. Leo, et al., Strategies for reducing speckle noise in digital holography, *Light Sci. Appl.* 7 (1) (2018) 1–16.
- [38] L. Gagnon, A. Jounan. Speckle filtering of SAR images: a comparative study between complex-wavelet-based and standard filters. *Wavelet Applications in Signal and Image Processing V.* 1997. 3169, 80-91.
- [39] G. D. Yue, Z. Xu, L. D. Wang, et al. Vibration analysis for slab track at different train speeds using Bayes wavelet denoising. *Proceedings of the Institution of Mechanical Engineers, Part F: Journal of Rail and Rapid Transit.* 2017. 231(8), 892-901.
- [40] C. Shen, R. Dollevoet, Z. Li, Fast and robust identification of railway track stiffness from simple field measurement, *Mech. Syst. Sig. Process.* 152 (2021), 107431.
- [41] M. Naeimi, Z. Li, R.H. Petrov, et al., Development of a new downscale setup for wheel-rail contact experiments under impact loading conditions, *Exp. Tech.* 42 (1) (2018) 1–17.
- [42] P. Zhang, J. Moraal, Z. Li, Design, calibration and validation of a wheel-rail contact force measurement system in V-Track, *Measurement* 175 (2021), 109105.
- [43] J. Lin, L. Qu, Feature extraction based on Morlet wavelet and its application for mechanical fault diagnosis, *J. Sound Vib.* 234 (1) (2000) 135–148.
- [44] S.G. Mallat, A theory for multiresolution signal decomposition: The wavelet representation, *IEEE Trans. Pattern Anal. Mach. Intell.* 11 (7) (1989) 674–693.
- [45] C. Bilen, S. Huzurbazar, Wavelet-based detection of outliers in time series, *J. Computat. Graph. Statist.* 11 (2) (2002) 311–327.
- [46] A. Grané, H. Veiga, Wavelet-based detection of outliers in financial time series, *Comput. Stat. Data Anal.* 54 (11) (2010) 2580–2593.
- [47] D. del Ser, O. Fors, J. Núñez, TFAW: Wavelet-based signal reconstruction to reduce photometric noise in time-domain surveys, *Astron. Astrophys.* 619 (2018) A86.

- [48] I. Pratama, A.E. Permasari, I. Ardiyanto, et al., A review of missing values handling methods on time-series data, in: 2016 International Conference on Information Technology Systems and Innovation (ICITSI), 2016, pp. 1–6.
- [49] F. Qu, J. Liu, Y. Ma, et al., A novel wind turbine data imputation method with multiple optimizations based on GANs, *Mech. Syst. Sig. Process.* 139 (2020), 106610.
- [50] H.N. Akouemo, R.J. Povinelli, Time series outlier detection and imputation, in: 2014 IEEE PES General Meeting| Conference & Exposition, 2014, pp. 1–5.
- [51] H. Liu, S. Shah, W. Jiang, On-line outlier detection and data cleaning, *Comput. Chem. Eng.* 28 (9) (2004) 1635–1647.
- [52] V. Layanun, S. Suksamosorn, J. Songsiri, Missing-data imputation for solar irradiance forecasting in Thailand, in: 2017 56th Annual Conference of the Society of Instrument and Control Engineers of Japan (SICE), 2017, pp. 1234–1239.
- [53] G.E. Box, G.M. Jenkins, G.C. Reinsel, et al., *Time series analysis: forecasting and control*, John Wiley & Sons, 2015.
- [54] I. Chang, G.C. Tiao, C. Chen, Estimation of time series parameters in the presence of outliers, *Technometrics* 30 (2) (1988) 193–204.
- [55] R.H. Jones, Maximum likelihood fitting of ARMA models to time series with missing observations, *Technometrics* 22 (3) (1980) 389–395.
- [56] S.F. Wu, C.Y. Chang, S.J. Lee, Time series forecasting with missing values, in: 2015 1st International Conference on Industrial Networks and Intelligent Systems (INISCom), 2015, pp. 151–156.
- [57] H. Akaike, A new look at the statistical model identification, *IEEE Trans. Autom. Control* 19 (6) (1974) 716–723.
- [58] S. Butterworth, On the theory of filter amplifiers, *Wirel. Eng.* 7 (6) (1930) 536–541.
- [59] G. Bianchi, R. Sorrentino, *Electronic filter simulation & design*, McGraw Hill Professional, 2007.
- [60] J. Lyu, X. Cai, M. Molinas, Frequency domain stability analysis of MMC-based HVDC for wind farm integration, *IEEE J. Emerg. Select. Top. Power Electron.* 4 (1) (2015) 141–151.
- [61] B. Amrouche, X. Le Pivert, Artificial neural network based daily local forecasting for global solar radiation, *Appl. Energy* 130 (2014) 333–341.
- [62] H. Demirhan, Z. Renwick, Missing value imputation for short to mid-term horizontal solar irradiance data, *Appl. Energy* 225 (2018) 998–1012.
- [63] A.S. Dhevi, Imputing missing values using inverse distance weighted interpolation for time series data, in: 2014 Sixth international conference on advanced computing (ICoAC), 2014, pp. 255–259.
- [64] P. Zhang, F. Li, A new adaptive weighted mean filter for removing salt-and-pepper noise, *IEEE Signal Process Lett.* 21 (10) (2014) 1280–1283.
- [65] Y. Wen, B. Zeng, A simple nonlinear filter for economic time series analysis, *Econ. Lett.* 64 (2) (1999) 151–160.
- [66] T. Nodes, N. Gallagher, Median filters: Some modifications and their properties, *IEEE Trans. Acoust. Speech Signal Process.* 30 (5) (1982) 739–746.
- [67] J.-S. Lee, Speckle suppression and analysis for synthetic aperture radar images, *Opt. Eng.* 25 (5) (1986) 255636.
- [68] J.-S. Lee, A simple speckle smoothing algorithm for synthetic aperture radar images, *IEEE Trans. Syst., Man Cybernet. SMC-13* (1) (1983) 85–89.
- [69] Q. Pan, L. Zhang, G. Dai, et al., Two denoising methods by wavelet transform, *IEEE Trans. Signal Process.* 47 (12) (1999) 3401–3406.
- [70] C. Shakher, R. Kumar, S.K. Singh, et al., Application of wavelet filtering for vibration analysis using digital speckle pattern interferometry, *Opt. Eng.* 41 (1) (2002) 176–180.